

# Low-Field Dedicated and Desktop Magnetic Resonance Imaging Systems for Agricultural and Food Applications

A. Constantinesco,<sup>1\*</sup> P. Choquet,<sup>1</sup> G. Cauffet,<sup>2</sup> J. M. Fournier,<sup>2</sup> S. Ravier,<sup>1</sup> J. M. Drillon<sup>3</sup> and G. Aubert<sup>4</sup>

<sup>1</sup> Laboratoire de Biomécanique, CHU Hautepierre, 1 Avenue Molière, 67098 Strasbourg, France

<sup>2</sup> LIME, UJF, BP 53 X, 38041 Grenoble Cedex 9, France

<sup>3</sup> IPCMS, 21 Rue Becquerel, 67000 Strasbourg, France

<sup>4</sup> CNRS Direction, 1 Rue Michel Ange, 75116 Paris, France

Dedicated low-field (0.1 T) resistive magnets equipped with solenoid coils were devised for high-resolution and rapid magnetic resonance imaging (MRI) in agricultural and food science. The maximum pixel resolution is  $0.1 \times 0.1$  mm with a 0.8 mm slice thickness, and 3D  $T_1$ ,  $T_2$  and  $T_2^*$  weighted images are obtained in 3 s–6 min depending on the contrast and number of slices. In place of resistive magnets two desktop permanent magnet designs are also described and their field characteristics and possible usefulness for small-sized low-cost MRI scanners, are discussed. © 1997 John Wiley & Sons, Ltd.

*Magn. Reson. Chem.* 35, S69–S75 (1997) No. of Figures: 10 No. of Tables: 5 No. of References: 32

**Keywords:** Low-field small magnetic resonance imaging; dedicated magnetic resonance imaging; resistive magnet; permanent magnet; food science

Received 12 April 1997; revised 30 May 1997; accepted 10 June 1997

## INTRODUCTION

The usefulness of nuclear magnetic resonance imaging (MRI) in the non-destructive analysis of biological systems has been widely demonstrated. Applications of the technique in food science have been tested by whole body medical imaging systems or, in some cases, laboratory research imaging systems. The purposes of the studies were the investigation of physiological mechanisms in plants<sup>1–3</sup> or food texture and transformation processes.<sup>4,5</sup> Results of such tests, confirming the interest of MRI in food science, were rarely obtained at low or mid-field<sup>6–8</sup> but generally with magnets of high field strengths of 2 T or more,<sup>9,10</sup> supposing that high spatial resolution can only be obtained at high field strength. The limitations of high-field MRI in agricultural and food science have been discussed.<sup>11</sup> The limitations are essentially in the cost and the installation constraints due to the use of expensive high-field superconducting magnets.<sup>12</sup> In this respect, the use of small, low-field magnets is a possible solution. Major problems to be solved concerning the use of low-field magnets are the demonstration of sub-millimetre spatial resolution and also short acquisition times aimed to industrial process control. Small resistive and permanent magnet techniques are able to overcome the major obstacles for MRI in food applications where high-field medical MRI

scanners are unsuitable not only with respect to cost, weight and susceptibility artefacts but also bulky installations. In agricultural and food industries, small-sized, specially designed and low-cost dedicated machines are desirable.

After a preliminary work on a 0.094 T NMR spectrometer,<sup>13</sup> we developed a dedicated 0.1 T low-field MR imaging system using a resistive magnet and the first images were obtained in 1990.<sup>14,15</sup> In this paper we present results on food imaging which were obtained with two differently designed dedicated resistive 0.1 T MRI scanners and discuss high-resolution and rapid imaging capabilities. We also describe preliminary work on another low-field magnetic source using permanent magnets designed for 'desktop' systems which may be more adaptable to industrial environments.

## EXPERIMENTAL

### Dedicated small MRI systems with devised resistive magnets

**Magnets and gradient coils.** We used two water-cooled resistive magnets (Drusch, Poissy, France) with a transverse (either vertical or horizontal) low magnetic field of 0.1 T [Fig. 1 (a) and (b)] whose characteristics are given in Table 1. Of particular interest is that the imaging zone of these two resistive magnets is accessible from three sides because the two pole pieces are connected by

\* Correspondence to: A. Constantinesco.  
Contract grant sponsor: Université Joseph Fourier.

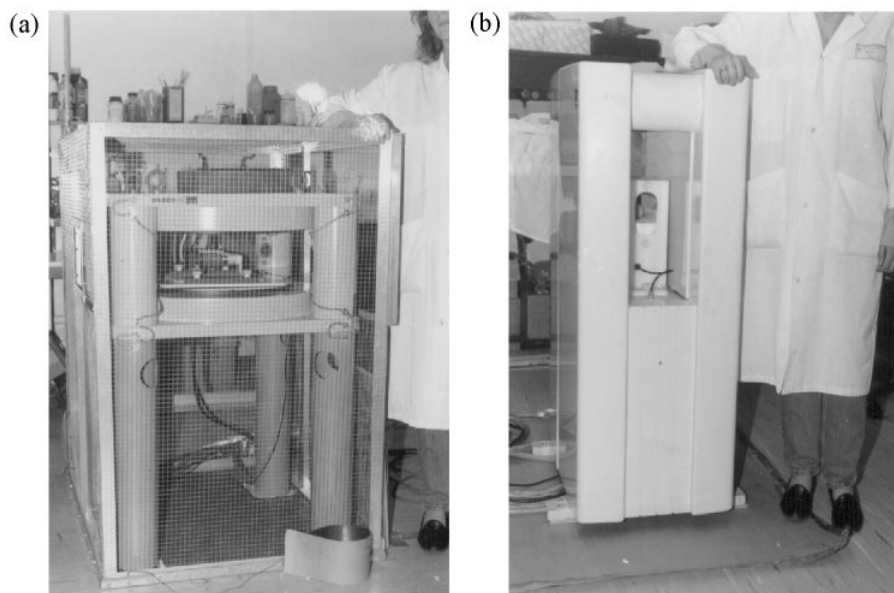


Figure 1. Resistive magnets for dedicated MR imaging systems. (a) Vertical field; (b) horizontal field.

Table 1. Characteristics of the two resistive magnets

Parameter	Vertical field	Horizontal field
Bearing surface area (m <sup>2</sup> )	0.49 (70 × 70 cm)	0.40 (56 × 72 cm)
Height (m)	1.03	1.18
Weight (kg)	700	850
Air gap (cm)	15	17
Power supply (kVA)	1.7	1.7
Water cooling (l min <sup>-1</sup> )	4	4

four columns. The field homogeneity (20 ppm) is improved by eight electrical current shims to 10 ppm in the imaging zone of an ellipsoid of 10 cm diameter by 6 cm height. The imaging gradients reach 20 mT m<sup>-1</sup> with a rise time of less than 1 ms. A Faraday cage can be installed to lessen the influence of the radioelectric environment as shown in Fig. 1(a).

**Radiofrequency coils** The orientation of the field allows the use of solenoidal radiofrequency (r.f.) coils with a good signal-to-noise (S/N) ratio and r.f. pulse homogeneity.<sup>16</sup> We have developed various transmitter-receiver coils with copper tubing or wire, pure solenoidal, loop-array type or conical coils depending on the size of the object to be imaged.<sup>17,18</sup> The dimensions and quality factors ( $Q$ ) of the r.f. coils are given in Table 2.

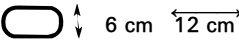
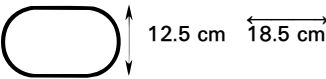

The r.f. coils are tuned at 4.26 MHz, which is the proton Larmor frequency at 0.1 T with fixed (American Technical Ceramics, New York, USA) and variable (Voltronics, NJ, USA) capacitances. The r.f. coils are none or less sensitive to the load and they have a quality factor ranging from 140 to 470 when they are unloaded and from 140 to 280 when they are loaded (all values were measured in the magnets). The smallest coils are, however, insensitive to the load.

We verified the homogeneity of the r.f.  $B_1$  field using the MISSTEC imaging sequence which produces an image of the  $B_1$  map.<sup>19</sup> A typical homogeneity map of

the r.f. field produced in the conical r.f. coil is shown in Fig. 2.

**The MRI console and imaging software.** The MRI console consisted of a 486 microcomputer with 4 Mb RAM equipped with specially devised boards (SMIS MR 3030, Surrey, UK). The imaging software was developed

Table 2. Dimensions and  $Q$  factors of the r.f. transmitter-receiver coils

Opening	Length (cm)	Loaded $Q$ factor (in magnet)
<i>Solenoidal coils:</i>		
○ $\phi$ 2 cm	5.7	209
○ $\phi$ 10 cm	9	273
<i>Loop-array coils:</i>		
 6 cm 12 cm	12	281
 12.5 cm 18.5 cm	13	260
<i>Conical coil:</i>		
2.4 cm  5.5 cm	10.5	171

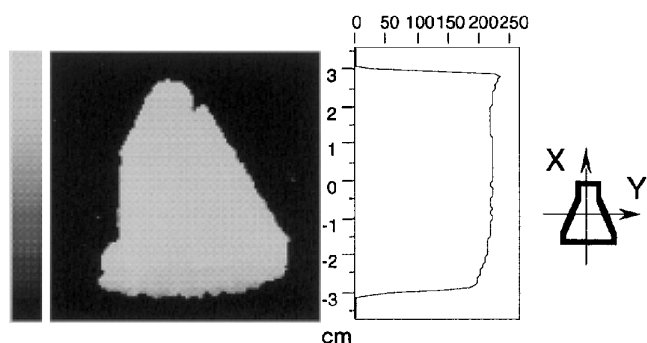


**Figure 2.** Mid-slice  $B_1$  field image of the conical coil and corresponding intensity profile along the  $x$ -axis.

in our laboratory. The MRI sequences are written in a C-like language using SMIS macros to define the shape and duration of the gradients and the r.f. pulses. The acquisition, processing and display functions and the screen management functions are written in Microsoft C v6.0 under DOS 5.0. The low magnetic field of 0.1 T requires careful improvement of the S/N ratio. We developed a 3D acquisition module to explore a whole object in a single acquisition with an increased S/N ratio. A set of 3D images data are acquired at the same time in place of 2D image data with a series of slice sections to avoid excessive signal reduction due to selective excitation. We introduced asymmetric,  $48 \times 64$ ,  $96 \times 128$  and  $192 \times 256$ , data acquisition matrices to reduce the acquisition time for one plane, which are further zero

filled to obtain a square matrix before Fourier transformation. For eight  $96 \times 128$  slices, the reconstruction time is less than 5 s.

In addition,  $48 \times 128$  and  $96 \times 256$  data acquisition matrices are zero filled to obtain asymmetric  $64 \times 128$  and  $128 \times 256$  reconstructed matrices, respectively, suitable for food morphologies and sagittal slices of long and thin objects. We implemented a wide range of sequences giving proton density,  $T_1$ ,  $T_2$  or  $T_2^*$  weighted contrasts, which are known as fast imaging sequences. Using a suitable sequence, choosing optimum parameters and accumulating several acquisition transients, images with high contrast were obtained.<sup>20</sup>

### Desktop permanent magnet prototypes

In agricultural and food applications, in some cases the dedicated MRI systems of resistive magnets are not suitable for industrial environments, owing, for instance, to their power supplies. Therefore, we developed another 0.1 T low magnetic field source using permanent magnets for small-sized desktop MRI scanners. Two prototypes using ferrite ceramics (Spinalor 4H, Ugimag, Grenoble, France) are under development. The first one, based on a patent by Aubert,<sup>21</sup> is a yokeless magnet made of two pole pieces with two concentrically arranged ring blocks of permanent magnetic material. The analytically calculated field inhomogeneity is 1 ppm in a cavity sphere whose diameter is half of the air

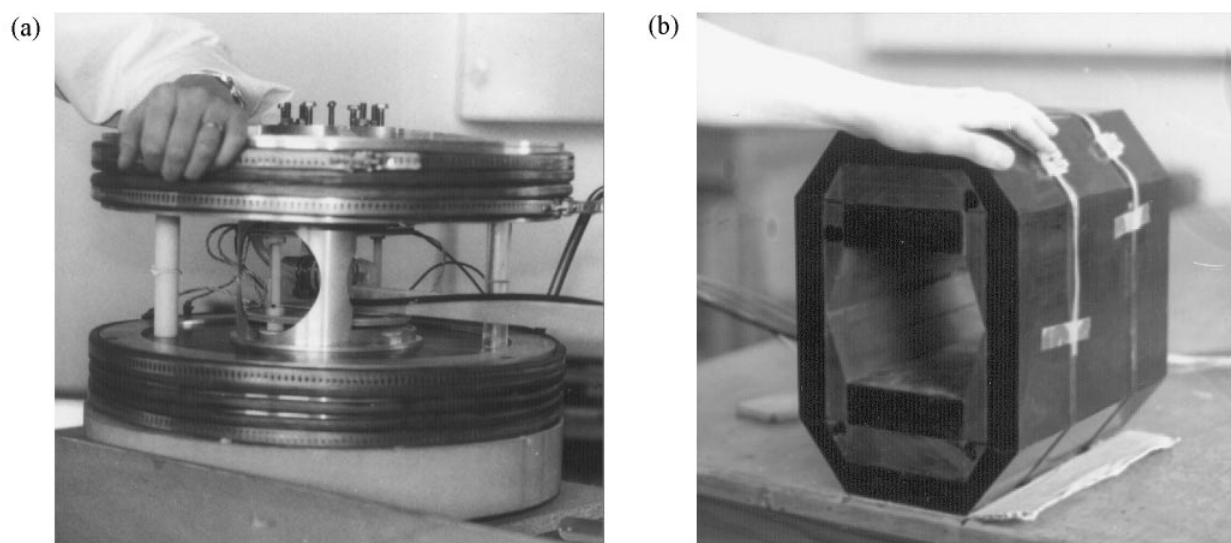


**Figure 3.** Desktop permanent magnets. (a) Aubert prototype; (b) cylinder prototype.

**Table 3.** Characteristics of the permanent desktop prototypes

Parameter	Aubert <sup>21</sup> prototype	Cylinder prototype
Bearing surface area (m <sup>2</sup> )	0.11 ( $\phi$ 38 cm)	0.066 (22 $\times$ 30 cm)
Height (cm)	23	32
Weight (kg)	30	60
Air gap (cm)	11	12
Ferrite ceramics remanence at 20 °C (T)	0.370	0.370
Ferrite ceramics coercity at 20 °C (kA m <sup>-1</sup> )	270	270
Expected imaging volume	5 cm sphere	5 cm sphere

gap. In practice, the field homogeneity depends on the position of the inner rings relative to the outer rings. An advantage of this structure is its open accessibility to the imaging zone [Fig. 3(a)]. The second prototype (cylinder prototype) has a polygon-shaped cavity made with a ring arrangement of uniformly magnetized prisms, a carbon steel yoke and two pole pieces to improve the field homogeneity, [Fig. 3(b)].<sup>22</sup> In both magnets, the magnetic field is oriented transversely, allowing the use of the same gradient and solenoid coil designs as developed previously for the resistive magnets. The general characteristics of the two desktop prototypes are given in Table 3.

## RESULTS

### Rapid high-resolution images obtained with the dedicated resistive magnet MRI systems

Fast gradient echo sequences are based on the steady-state free precession principle.<sup>23</sup> A short pulse repetition time ( $TR$ ) establishes a steady-state magnetization in both longitudinal and transverse planes. By appropriately alternating imaging gradients they provide variable contrasts in rapid examinations. The FAST and CE-FAST sequences<sup>24</sup> generate  $T_1$  and  $T_2$  weighted images, respectively, with a  $TR$  between 20 and 60 ms, (Figs 4–6). The FLASH sequence<sup>25</sup> provides either proton density,  $T_1$  or  $T_2^*$  weighted contrasts, depending on the  $TR$ , the  $TE$  and the flip angle, (Fig. 5). Using given  $TR$  and flip angle, multi- $T_2^*$  weighted images are obtained by rephasing the spins by inverting the encoding gradient, to generate a second echo. Two sets of images with different contrasts are then acquired in the same time. The careful choice of these sequence parameters is essential for obtaining images of high S/N ratio because these sequences generate less signal than sequences with longer  $TR$ .<sup>20</sup> The images are degraded by field inhomogeneities but the effect is less important with low magnetic fields.<sup>26</sup> Finally, the short  $TR$

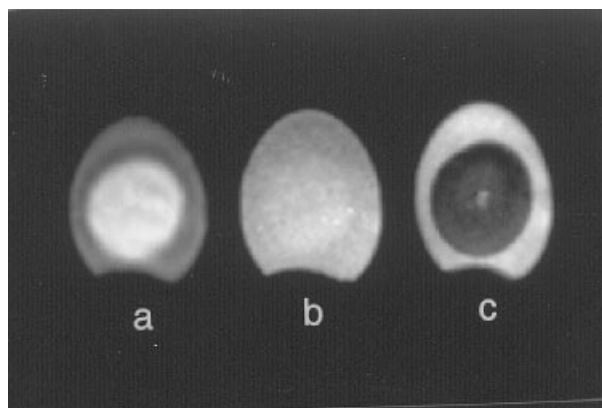


**Figure 4.** Slices No. 2 of an egg from three series of four contiguous slices showing variations of the  $T_2$  weighted contrast obtained with a FAST sequence with different values of  $TE$ . Resolution,  $0.8 \times 0.8$  mm per pixel; thickness, 3 mm; FOV, 51 mm; total acquisition time (four slices), 46 s. FAST sequence ( $TR/TE/FA$ ): (a) 60/7/65°; (b) 60/9/65°; (c) 60/20/65°.

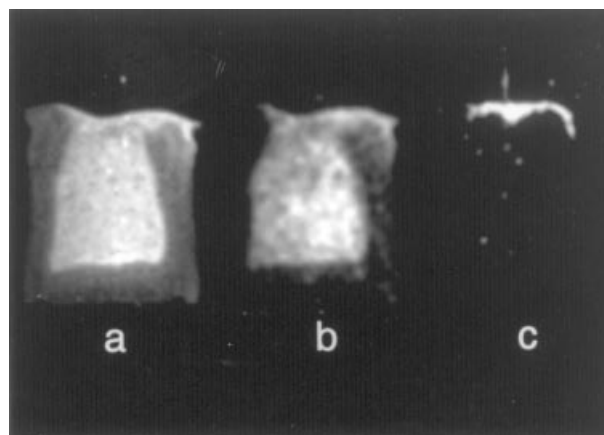


**Figure 5.** Slices No. 4 of a small meat pie from three series of eight contiguous slices showing short  $T_1$ , long  $T_1$  and  $T_2$  weighted contrasts. (a) Short  $T_1$  weighted contrast with a FLASH sequence 400/4/90°. Resolution,  $0.5 \times 0.5$  mm per pixel; thickness, 5 mm; FOV, 64 mm; total acquisition time (eight slices), 5 min 7 s. (b) Long  $T_1$  weighted contrast with a FAST sequence 60/9/65°. Resolution,  $0.5 \times 0.5$  mm per pixel; thickness, 5 mm; FOV, 64 mm; total acquisition time (eight slices), 1 min 32 s. (c)  $T_2$  weighted contrast with a CE-FAST sequence 29/22/35°. Resolution,  $0.5 \times 0.5$  mm per pixel; thickness, 5 mm; FOV, 64 mm; total acquisition time (eight slices), 45 s.

method allows averaging of more accumulated transients for improving the S/N ratio than the long  $TR$  methods to compensate for the reduced signal intensity.

Spin-echo sequences are useful for  $T_2$  investigations but the long  $TR$  required of 2 s or more is time consuming, even at low field where  $T_1$  is decreased, allowing shorter  $TR$ . RARE sequence<sup>27</sup> encodes several lines or slices during the same  $TR$  with multi-echoes, which reduces the spin-echo examination time. Because not all the lines of a data set come from the same echo, artefacts due to the  $T_2$  signal decay between successive echoes occur. The artefacts can be minimized and rejected in the slice direction if slice encoding is done with the same echo in each excitation (Fig. 7). More or less  $T_2$  weighted investigations are therefore realised in about 3 min with the RARE sequence. Table 4 describes some sequence parameters and total corresponding imaging times.

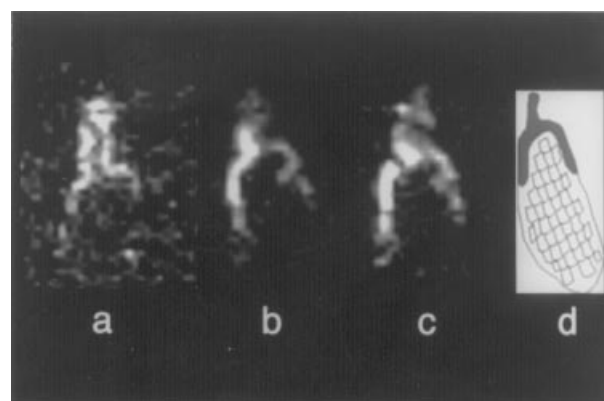


**Figure 6.** Rehydration of a dried morel, long  $T_1$  weighted contrast obtained with a FAST sequence 40/9/75°. Resolution,  $0.8 \times 0.8$  mm per pixel; thickness, 5 mm; FOV, 51 mm; total acquisition time (four slices), 31 s. (a) First image,  $t_0$ ; (b)  $t_0 + 5$  min; (c)  $t_0 + 10$  min; (d) drawing of the morel being rehydrated.



**Figure 7.** One slice from 16 slices of a kiwi fruit obtained with a RARE sequence 2000/100/90° ( $T_2$  weighted). Resolution,  $0.35 \times 0.35$  mm per pixel; thickness, 5 mm; FOV, 44.8 mm; total acquisition time (16 slices), 6 min 24 s.

With the above sequences and our coils, a 0.1 mm per pixel in-plane resolution with slice thicknesses of 0.8 mm is attained (Fig. 8). Table 5 shows the adequate combinations between the field of view (FOV), the matrix size and the acquisition time.

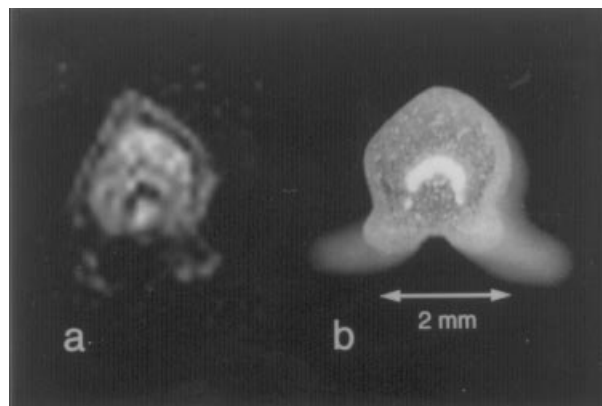


**Figure 8.** Transverse slice of the petiole of a leaf. (a) High-resolution  $T_1$  weighted MR image with a FLASH sequence 200/15/90°. Resolution,  $100 \times 100$   $\mu$ m per pixel; thickness, 800  $\mu$ m; FOV, 6.4 mm; total acquisition time (eight slices), 40 min. (b) Corresponding picture of the stem.

In routine use, the total acquisition time for eight contiguous slices with an in-plane pixel resolution of  $0.4 \times 0.4$  mm does not exceed 3 min.

#### Field characteristics of the two desktop permanent magnet prototypes

Major problems in the use of permanent magnets for MRI are the poor temporal field stability due to the

**Table 4.** Routine sequence parameters, in-plane resolution and acquisition times for contiguous slices of 3 mm in a 3D acquisition mode

3 D sequences	TR (ms)	TE (ms)	mm per pixel	Matrix	NEX <sup>a</sup>	Total acquisition time
Spin-echo ( $T_2$ )	1500	80	0.8	$128 \times 96$	1	9 min 36 s
4 slices						
RARE ( $T_2$ ) <sup>b</sup>	2000	100	0.8	$128 \times 96$	2	6 min 24 s
8 slices						
CE-FAST ( $T_2$ ) <sup>b</sup>	20	9	0.8	$128 \times 96$	2	16 s
4 slices						
CE-FAST ( $T_2$ ) <sup>b</sup>	29	22	1.6	$64 \times 48$	1	6 s
4 slices						
FLASH ( $T_1$ ) <sup>b</sup>	200	10/20	0.8	$128 \times 96$	2	2 min 34 s
4 slices						
FAST ( $T_1$ ) <sup>b</sup>	60	9	0.8	$128 \times 96$	2	46 s
4 slices						
FAST ( $T_1$ ) <sup>b</sup>	16	9	1.6	$64 \times 48$	1	3 s
4 slices						

<sup>a</sup> Number of transients accumulated.

<sup>b</sup> Weighted.

**Table 5.** Acquisition time for a given field of view with different matrix sizes<sup>a</sup>

	Field of view (mm)	Data matrix size	In-plane resolution (pixel size in mm <sup>2</sup> )	NEX <sup>b</sup>	Total acquisition time for 8 slices
Axial slices	$25 \times 25$	$48 \times 64$	$0.4 \times 0.4$	4	1 min 30 s
	$25 \times 25$	$96 \times 128$	$0.2 \times 0.2$	8	6 min
Sagittal slices	$25 \times 50$	$48 \times 128$	$0.4 \times 0.4$	4	1 min 30 s
	$50 \times 50$	$96 \times 128$	$0.4 \times 0.4$	4	3 min
	$25 \times 50$	$96 \times 256$	$0.2 \times 0.2$	8	6 min

<sup>a</sup> The excitations are given for eight contiguous slices of 2 mm thickness with the FAST sequence ( $TR = 60$  ms,  $TE = 9$  ms).

<sup>b</sup> Number of transients accumulated.

thermal field dependence of the magnetic material and the field homogeneity required for imaging. Regarding the former point, we found a high linear correlation ( $r = 0.998$ ) between the magnetic field  $B_0$  measured at the centre of the first prototype and temperature in the range 20–30 °C (Fig. 9). To perform this experiment, the prototype was installed in an adiabatic container and its temperature was regulated with  $\pm 0.1$  °C precision by a water thermostat. The observed relationship, therefore, can be used to monitor the thermal magnetic shift of ferrite ceramics, also taking advantage of the thermal inertia of the whole structure.<sup>28</sup>

Concerning the latter point, the measured field homogeneity of the first prototype [Fig. 3(a)], was 1500 ppm in a 5 cm sphere instead of the 50 ppm required for imaging. This can be greatly improved because it might be the summation of mechanical component tolerances and construction errors, particularly concerning the

relative displacements between the two rings of each pole which are adjustable. Figure 10 is a plot of the measured magnetic field  $B_0$  along the x-axis of the cylinder prototype [Fig. 3(b)]. One can see that the distribution is not symmetric. This is also due to imperfect fabrication and assembly of the ferrite ceramics. However, the field homogeneity over a distance of 5 cm around the centre of the magnet is 60 ppm. This result is very encouraging since no shimming corrections were made. The result indicates that with careful fabrication and assembly and also shimming corrections, the field homogeneity needed for imaging can be achieved.

## DISCUSSION AND CONCLUSION

We believe that the food and agricultural sciences need small-sized, open and robust MRI systems whose spatial resolution and acquisition time are comparable to those of mid- or even high-field MRI medical scanners. Among the possible magnetic field sources, we demonstrate that resistive magnets operating at 0.1 T have good performances when the r.f. coils are optimized and fast gradient echo or RARE<sup>27</sup> pulse sequences are used. However, even such systems are sometimes not suitable in an industrial environment owing to the cumbersome and power-hungry properties of resistive magnets. In this respect the permanent magnet approach offers a solution. The principal goal is to establish a larger imaging cavity using a small permanent magnet. Studies on various design structures showed significant discrepancies between calculated (either analytically or more often by finite element methods) and experimentally obtained field homogeneities.<sup>29</sup> Our preliminary results using yokeless and yoked desktop prototypes were in agreement with the results from other groups.<sup>11,12,30,31</sup> However, field homogeneity will be further improved by a careful mechanical assembly and by an appropriate magnetic dipole or electric shimming.<sup>22,28,32</sup> The interest of these low-field dedicated and desktop MRI systems lies in their low cost, which is estimated to be in the range

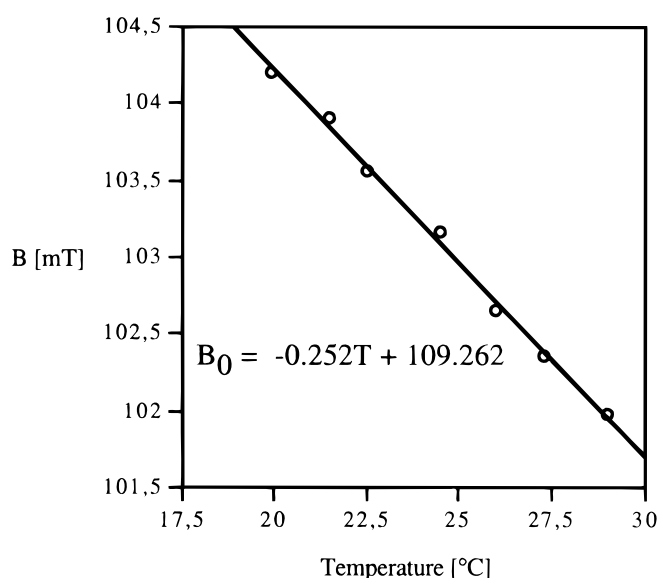


**Figure 9.** Linear correlation between the  $B_0$  field and temperature measured at centre of the prototype 1. The magnetic field was measured with a teslameter (RMN PT 2025, Metrolab, Geneva, Switzerland).

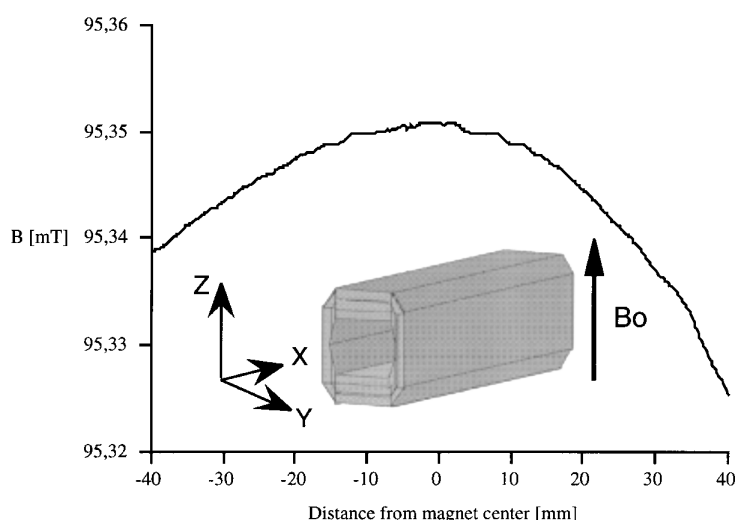


**Figure 10.** Distribution of measured magnetic field along the x-axis of the cylinder prototype. The magnetic field was measured with a teslameter (Metrolab RMN PT 2025).

\$100 000–200 000. This may be a great advantage regarding future applications of the technique. Moreover, at low field,  $T_1$  image contrast is improved and artefacts due to field strength such as chemical shifts or susceptibility associated with high-field MRI are avoided. The signal itself is, of course, weak but short  $TR$  can be used because of shortening of the apparent longitudinal relaxation time and more averaging is possible. This results in an increase in the S/N ratio. These small-sized MRI scanners permit rapid non-destructive examinations in industrial environments and changes in

some decision trees in industrial processes. Small, dedicated systems may lead to many new MRI applications, in the agricultural and food sciences.

### Acknowledgements

The authors thank SERAS-CNRS for the design and realization of the prototype based on Aubert's patent, the Université Joseph Fourier for financial support and Apple Computer France for help. The authors also thank M. G. Vetter for technical help.

### REFERENCES

1. J. H. Brown, G. A. Johnson and P. J. Kramer, *Plant Physiol.* **82**, 1158 (1986).
2. K. Omasa, M. Onoe and H. Yamada, *Environ. Control Biol.* **23**, 99 (1985).
3. P. Chen, M. J. McCarthy, R. Kauten, Y. Sarig and S. Han, *J. Agric. Eng. Res.* **55**, 177 (1993).
4. H. Song and J. B. Litchfield, *Cereal Chem.* **67**, 580 (1990).
5. S. L. Duce and L. D. Hall, *J. Food Eng.* **26**, 251 (1995).
6. A. Alanen, M. Komu, S. Bondestam and S. Toikkanen, *Phys. Med. Biol.* **36**, 953 (1991).
7. S. A. Naik, R. S. Chaugule, R. Vijayaraghavan, S. S. Ranade and N. C. Shah, *J. Magn. Reson. Anal.* **1**, 49 (1995).
8. S. Y. Wang, P. C. Wang and M. Faust, *Sci. Hort.* **35**, 227 (1988).
9. S. L. Duce, T. A. Carpenter and L. D. Hall, *J. Food Eng.* **16**, 165 (1992).
10. B. A. Goodman, B. Williamson, E. J. Simpson, J. A. Chudek, G. Hunter and D. A. M. Prior, *Magn. Reson. Imaging* **14**, 187 (1996).
11. F. E. Bertora and M. G. Abele, *Magn. Reson. Imaging* **10**, 809 (1992).
12. S. I. Cho, G. W. Krutz, H. G. Gibson and K. Haghighi, *Trans. Asae* **33**, 1043 (1990).
13. P. Gries and A. Constantinesco, *J. Biophys. Bioméca.* **11**, 139 (1987).
14. P. Gries, A. Constantinesco, C. Ortlieb, S. Pittard, B. Brunot, W. Vennart, J. Demangeat and R. Ellis, *J. Med. Nucl. Biophys.* **14**, 343 (1990).
15. P. Gries, A. Constantinesco, B. Brunot and A. Facello, *Magn. Reson. Imaging* **9**, 949 (1991).
16. D. I. Hoult and R. E. Richards, *J. Magn. Reson.* **24**, 71 (1976).
17. C. Leussler and W. Vollmann, in *Proceedings of SMRM, Amsterdam*, p. 938. SMRM, Berkeley (1989).
18. L. Sun, J. O. Olsen and P. M. L. Robitaille, *Magn. Reson. Imaging* **11**, 73 (1993).
19. S. Akoka, F. Franconi, F. Seguin and A. LePape, *Magn. Reson. Imaging* **11**, 437 (1993).
20. S. Arbogast-Ravier, F. Xu, P. Choquet, B. Brunot and A. Constantinesco, *Med. Biol. Eng. Comput.* **33**, 735 (1995).
21. G. Aubert, *US Pat.* 5 332 971 (1994).
22. Z. X. Feng, X. H. Jiang and S. Han, *IEEE Trans. Magn.* **28**, 641 (1992).
23. H. Y. Carr, *Phys. Rev.* **112**, 1693 (1958).
24. M. L. Gyngell, *Magn. Reson. Imaging* **6**, 415 (1988).
25. J. Frahm, A. Haase and D. Matthaei, *J. Comput. Tomogr.* **10**, 363 (1986).
26. F. A. Jolesz and S. Patz, *Magn. Reson. Imaging* **6**, 397 (1988).
27. J. Hennig, A. Naureth and H. Friedburg, *Magn. Reson. Med.* **3**, 823 (1986).
28. P. Schuster, PhD Thesis, Grenoble (1986).
29. V. Nguyen, PhD Thesis, Grenoble (1996).
30. R. Z. Zhou, K. W. Wang and S. Han, in *Proceedings of the 11th International Conference on Magnet Technology*, p. 1271. Elsevier, London (1990).
31. J. H. Battocletti and T. A. Knox, *IEEE Trans. Magn.* **5**, 1874 (1985).
32. H. Sakurai, M. Aoki and T. Miyamoto, *IEEE Transl. J. Magn. Jpn.* **6**, 524 (1991).